Scaling of Silicon Nanoparticle Growth in Low Temperature Flowing Plasmas

Steven J. Lanham[1], Jordyn Polito[1], Xuetao Shi[2], Paolo Elvati[2], Angela Violi[1,2], and Mark J. Kushner[1,3,4]

[1] Department of Chemical Engineering, University of Michigan, 1301 Beal Ave., Ann Arbor, MI 48109-2122 USA, sjlanham@umich.edu, jopolito@umich.edu

[2] Department of Mechanical Engineering, University of Michigan, 1301 Beal Ave., Ann Arbor, MI 48109-2122 USA, xuetao.shi@wayne.edu, elvati@umich.edu, avioli@umich.edu

[3] Department of Electrical Engineering and Computer Science, University of Michigan, 1301 Beal Ave., Ann Arbor, MI 48109-2122 USA, mjkush@umich.edu

[4] Author to whom correspondence should be addressed.

Abstract

Low temperature plasmas are an emerging method to synthesize high quality nanoparticles (NPs). An established and successful technique to produce NPs is using a capacitively coupled plasma (CCP) in a cylindrical geometry. Although a robust synthesis technique, optimizing or specifying NP properties using CCPs is challenging. In this paper, results from a computational investigation for growth of silicon NPs in flowing inductively coupled plasmas (ICPs) using Ar/SiH_4 gas mixtures of up to a few Torr are discussed. ICPs produce more locally constrained and quiescent plasma potentials. These positive plasma potentials produce an electrostatic trap for negatively charged NPs which can significantly extend the residence time of NPs in the plasma, which in turn provides a controllable period for particle growth. The computational platforms used in this study consist of a 2-dimensional plasma hydrodynamics model, a 3-dimensional nanoparticle growth and trajectory tracking model and a molecular dynamics simulation for deriving reactive sticking coefficients of silane radicals on Si NPs. Trends for nanoparticle growth as a function of SiH_4 inlet fraction, gas residence time, energy deposition per particle, pressure, and reactor diameter are discussed. The general path for particle synthesis is trapping of small NPs in the positive electrostatic potential, followed by entrainment in the gas flow upon reaching a critical particle size. Optimizing or controlling NP synthesis then depends on the spatial distribution of plasma potential, density of growth species, and the relative time that particles spend in the electrostatic trap and flowing through higher densities of growth species upon leaving the trap.

I. Introduction

Low temperature plasmas are keen alternatives to traditional liquid phase methods for synthesis of nanoparticles due to the unique nonthermal plasma environment [1]. Plasmas are particularly useful for synthesis of nanoparticles (diameters of a few to 10s of nm) composed of high melting point materials that require crystallization temperatures above which can be sustained in liquid solvents [2]. Plasmas also enable synthesis of compound nanoparticles (NPs) such as group III-V semiconducting materials and metal oxides that require covalent bonding rather than the ionic bonding promoted by liquid phase synthesis [3]. NPs synthesized in plasmas include: silicon nanoparticles with high photoluminescent yields, gold nanoparticles and nanostructures used for solar water splitting and enhancement of solar cells, doped copper sulfide and titanium nitride nanoparticles with extended plasmonic range for use in photocatalysis, gallium nitride nanoparticles for electroluminescent and power electronics, and zinc oxide nanoparticles for use in cancer treatment, among others [4–8]. Plasma produced NPs have properties (size, luminescence, hardness, and composition) that are tunable by changing plasma operating parameters such as power, pressure, gas flow rate, excitation method and gas composition [9–11]. Understanding the relationship between plasma operating parameters and particle growth, morphology, and composition will lead to optimization of plasma nanoparticle production techniques and enable rapid development of new and novel nanomaterials.

Nanoparticles have been synthesized in a variety of radio frequency (RF) or DC driven reactor configurations by flowing small fractions of a metal-containing precursor gas, such as silane (SiH_4) for Si nanoparticle production, in a carrier gas such as argon or helium. The precursor gas is then dissociated by electron impact processes creating radicals in the plasma, leading to nanoparticle growth by nucleation, agglomeration and eventually surface deposition. A three-step growth mechanism has been widely accepted for plasma produced nanoparticles, though not all aspects are fully understood. Boufendi and Bouchoule showed that plasma-assisted nanoparticle synthesis occurs by nucleation, coagulation, and growth by surface deposition [12]. The nucleation phase is characterized by a rapid increase in particle size and decrease in particle concentration, resulting in crystalline particles a few nm in size. The small particles coagulate, resulting in larger nanoparticles (~50 nm) that gain increasingly negative charge and become trapped in the center of the plasma where the electrical potential is highest. The growth of the trapped particles is dominated by surface deposition by radicals, and particles

with diameters from a few hundred nm to a few microns can be produced. Since particles of the same polarity repel each other, mechanisms for coagulation are among the most debated of the nanoparticle growth processes.

Particle charging is thought to be one of the most important factors contributing to the unique properties and morphologies of low temperature plasma (LTP) produced nanoparticles. Particles of sizes greater than a few nm in LTPs typically charge negatively, which prevents sometimes undesired agglomeration due to the NP mutual electrostatic repulsion, leading to a narrower size distribution compared with other synthesis methods. With most LTPs having a positive electrical potential, charging also results in particle trapping at the center of the plasma, which can facilitate more growth and heat nanoparticles to temperatures sufficient for crystallization [13]. Particle charge distributions are sensitive functions of plasma properties and may be one of the most useful NP properties for correlating nanoparticle growth to plasma operating conditions. The number of elementary charges on NPs span several orders of magnitude with small NPs (< 1 nm) having zero to a few negative elementary charges (and in some cases positive), while larger nano- and micron-sized particles having several thousands of negative elementary charges [14]. Monte Carlo simulations performed of particle charging showed that small particles in LTPs may also carry small positive charge with the rate of charge fluctuation decreasing with increasing particle size [15]. The charge on small NPs (< a few nm) have stochastic fluctuations that occur on time scales that are much shorter (10^5 - 10^6 s^{-1}) than the time for particle charge to reach equilibrium (a few ms).

Several computational investigations of LTP facilitated nanoparticle synthesis have been conducted while also facing several challenges. NPs are chemically reactive, nucleating, coagulating, and grow at different rates dependent on plasma parameters, such as gas mixture power and residence time, while local reactant densities can vary over the length of a reactor. The polydispersity of particle size distributions adds a level of complexity and computational burden. To address the large range of sizes of plasma produced NPs, many models employ a sectional growth approach, adapted from the aerosol physics community, in which the particle size range is divided into bins and a population balance is solved for each bin [14,16,17,18]. Each size bin may be further divided into different charge states. Due to the large number of equations needed to resolve the systems of interest, these models are computationally expensive and are often 0- or 1-dimensional. When including particle charge distributions in sectional

models, the computational burden increases. Monte Carlo (MC) methods have been used to address these computational scaling challenges, and have produced nano-particle size and charge distributions which agree very well with experiments [19]. With the emphasis on particle properties, these MC methods often specify the plasma conditions as opposed to computing the plasma conditions from first principles.

In this paper, we report on results from a computational investigation of silicon NP synthesis in flowing LTPs with the goals of clarifying how operating conditions in a cylindrical reactor affect plasma properties and the resulting impact this has on NP growth rates. The algorithms used here are less computationally intensive than sectional models [18] while agreeing systematically with their results. Simulations were performed of inductively coupled plasmas (ICP) sustained in Ar/SiH_4 mixtures in cylindrical reactors having diameters of up to 1.5 cm, pressures of 0.25 to 2.5 Torr and silane mole fractions of 0.1% to 50%. The computational platforms used in the study are a 2-dimensional hybrid-multi-fluid plasma model coupled with a 3-dimensional kinetic model for particle growth and tracking. Reactive sticking coefficients for silane radicals onto growing NPs were computed using molecular dynamics methods. The intent of this work is to assess how trapping of negatively charged particles in the positive plasma potential influences growth rates and particle size. The ICP system was chosen since for cylindrical reactors, the plasma potential is quiescent with locally defined maximum compared to, for example, capacitively coupled systems. We found that when negatively charged NPs become trapped near the peak in the plasma potential, the trapping time can span multiple gas residence times. The particles are de-trapped when they grow large enough that fluid drag forces begin to dominate, and the NPs flow out of the reactor. Growth continues as the NPs flow downstream through a region that is rich in growth precursors. The charging of the NPs is dynamic, negative and increasing in magnitude when trapped in the plasma, while discharging as they flow downstream.

The models used in this investigation are described in Section II. Trends for nanoparticle growth with SiH_4 inlet fraction, gas residence time, energy per particle, pressure, and reactor radius are discussed in Section III. Concluding remarks are in Section IV.

II. Description of the Models

The plasma chemistry and transport of growing nanoparticles in LTPs depend on multiple length and time scales. The investigations discussed here were performed by coupling a plasma hydrodynamics model [Hybrid Plasma Equipment Model (HPEM)] with a 3-dimensional kinetic model for growing nanoparticles [Dust Transport Simulator (DTS)]. Reactive sticking coefficients employed in the DTS were computed using molecular dynamic simulations.

A. Reactor Scale Plasma Chemistry Model

The reactor scale plasma chemistry and hydrodynamics were modeled using the Hybrid Plasma Equipment Model (HPEM), a two-dimensional multi-fluid plasma simulator, described in detail in Ref. [20]. Briefly, the HPEM uses a modular approach to address the relevant physics using a time slicing technique. In this work, the Electromagnetics Module (EMM) was used to compute azimuthal electric fields and their absorption in the plasma produced from an antenna powered at radio frequency (RF). Secondary electron emission from surfaces is addressed in the Electron Energy Transport Module (EETM), where a Monte Carlo simulation is used to track their trajectories and generate electron impact source functions. These source functions are used in the Fluid Kinetics Poisson Module (FKPM). The FKPM computes separate fluid continuity, momentum and temperature equations for each heavy species (neutrals and ions). Continuity and temperature equations are solved for electrons assuming a drift-diffusion formulation for momentum. Rate coefficients for the electron energy equation are obtained from local solutions of Boltzmann's equation for the electron energy distribution. Poisson's equation for the electric potential is solved semi-implicitly with each time step in the FKPM for self-consistency. The full set of equations are integrated for multiple gas residence times until a pseudo-steady state is reached.

The Ar/SiH_4 reaction mechanism used in this work is a concise version from the work by Picard *et al.* [18] with data from previous works [21,22]. The species included in the simulation are listed in Table 1. Particle growth is addressed in the DTS which feeds back to the FKPM the local values of NP density and charge on the NPs. These values are then used in the charge balance for solution of Poisson's equation, for the attachment (or neutralization) of electrons and ions on the NPs. In the DTS, the Havne's P-parameter [23–25] is much less than 1, meaning that the NP density is too low to significantly impact the electric potential in the reactor. For the conditions addressed here, the electronegativity parameter, α_0, the ratio of negative ions to

electrons [26], is ≈10 where power deposition is large in the vicinity of the antenna. α_0, increases to >1,000 downstream as the plasma flows out of the reactor. This large electronegativity decreases the impact of a low P-parameter.

B. DTS and Nanoparticle Growth Model

NP transport and growth were addressed using a 3-dimensional kinetic model, the DTS, embedded in the HPEM. The implementation described here is built on prior versions of the DTS [27,28] and the prior dust particle transport model [29]. The DTS obtains plasma properties from the HPEM, including electric fields, and species densities, temperatures, and momentum flux fields. The precursors to NPs are initialized randomly in the plasma and their trajectories are integrated based on the relevant forces: gravitational, electrostatic and inter-particle Coulomb forces, ion drag, viscous fluid drag, thermophoresis and Brownian motion. The forces on NP species i are,

$$\vec{F}_i = M_i\vec{g} + Q_i\vec{E} + \sum_j \vec{F}_{cij} + \sigma_{ion}\vec{\phi}_{ion}\left|\vec{v}_{ion}\right| - \frac{6\pi\mu r_i}{C(Kn)}\left(\vec{v}_i - \vec{u}_f\right)C_D\left(\mathrm{Re}_p\right)\frac{\mathrm{Re}_p}{24} - 6\pi\mu r_i \nu_f K_T \frac{\nabla T}{T_{gas}} + \vec{F}_B \,, \quad (1)$$

where $\vec{g}$ the gravitational acceleration, M_i is the mass of the NP, Q_i is the electrical charge of the NP, $\vec{E}$ is the electrostatic electric field, and $\vec{F}_{cij}$ is the Coulombic force between NP species *i* and *j*. The fourth, fifth, sixth, and seventh terms account for the forces due to ion drag, fluid drag, thermophoresis and Brownian motion, discussed below.

The charge on individual NPs is computed by integrating the current to the particle surface due to positive and negative ions, and electrons. The current to NP *i* due to positive ion *j*, I_{ij}^+, negative ion *k*, I_{ik}^-,and electrons I_{ie} are

$$I_{ij}^+ = \pi r_i^2 N_j^+ q\sqrt{\frac{2\varepsilon_{Ij}}{m_j}}\left(1 - \frac{q\Phi_i}{\varepsilon_j}\right), \quad (2)$$

$$I_{ik}^- = \pi r_i^2 N_k^- q\sqrt{\frac{8k_B T_-}{\pi m_k}}\exp\left(\frac{q\Phi_i}{k_B T_k}\right), \quad (3)$$

$$I_{ie} = \pi r_i^2 N_e q\sqrt{\frac{8k_B T_e}{\pi m_e}}\exp\left(\frac{q\Phi_i}{k_B T_e}\right), \quad (4)$$

where r_i is the radius of the NP; N_j, N_k and N_e are the densities of positive ion j, negative ion *k* and electrons; ε_j is the kinetic energy of ion *j*; T_k and T_e are the temperatures of negative ion *k* and electrons; m_j, m_k and m_e are the masses of positive ion *j*, negative ion *k* and electrons; k_B is Boltzmann's constant; and Φ_i is the floating electrical potential of NP *i*. These currents result from assuming Orbital Motion Limited (OML) trajectories for positive ions [30,31]. For small NPs (i.e., < a few to 10 nm), the currents collected by individual particles have significant stochastic components [15]. In addition to this stochastic charge collection, there is a computational complication. For small NPs when using a continuum approximation, the current flowing to the NP over a typical integrating time step produces less charge than a single electron or ion. Given these conditions, computing NP charge using continuous integration of currents to the particles is problematic.

To address these conditions, a stochastic charging algorithm was implemented. With this algorithm, the charge collected from the current of each ion or electron species during an integration time step is treated as the mean expected value of a Poisson distribution – used to describe discrete, rare events with an unknown variance. The Poisson distribution expresses the probability of discrete events occurring during a fixed time interval, and naturally arises as the limit of the binomial distribution with increasing number of trials. Sampling from this distribution is done using a sequential search algorithm [32] where a random number is generated and compared to the probability of i events occurring (P_i) with a mean μ,

$$P_i = \sum_{k=0}^{i-1} e^{-\mu} \mu^k / k! \quad (\text{i}=1,2,...) . \tag{5}$$

The algorithm is to generate a random number r = [0,1] and compute the P_i for increasing values of i until $r < P_i$. When the probability of the i^{th} event exceeds the random number, the number of events (N) is returned as N=i-1. The execution time for this algorithm increases with increasing μ, so for μ>5 the Poisson distribution is approximated as Gaussian with a variance equal to the mean. However, for the particle sizes and time steps used in this work, μ is small (typically < 1) and the assumptions needed for sampling from a Poisson distribution are valid. An example output using the stochastic charging algorithm is shown in Fig. 1. The relative fluctuations around the mean particle charge decreases with increasing particle size, corroborating that fluctuations are less important for larger sized particles. The frequency of oscillations increases with increasing particle size as current to the particle increases in magnitude, with particle charge

changing ~1q per ms for a 1 nm NP to charge varying 100s of q per ms for 100 nm particles.

With charge on the NP, Q_i, known, the floating electrical potential of the NP is obtained by assuming that the NP acts as spherical capacitor with capacitance C_i with a surrounding sheath having thickness given by the linearized Debye length, λ_L [33]:

$$\Phi_i = \frac{Q_i}{C_i},\ C_i = 4\pi\varepsilon_0 r_i\left(1+\frac{r_i}{\lambda_L}\right), \tag{5}$$

$$\frac{1}{\lambda_L} = \sqrt{\frac{q^2}{\varepsilon_0}\left(\frac{N_e}{k_B T_e}+\sum_k \frac{N_k^-}{k_B T_k}+\sum_k \frac{N_j^+}{2\varepsilon_j}\right)}. \tag{6}$$

In collisional plasmas, the ion trajectory around the NP predicted by the OML theory may be interrupted by a charge-exchange collision. This collision produces a low energy ion which can be directly collected by the NP, resulting in a higher ion current and less negative ion potential [34]. For the largest particles and highest pressures considered here, this additional ion current could make a contribution, but otherwise these collisional effects are not important.

The numerical mesh used to solve Poisson's equation in the fluid modules of the HPEM for the electric potential has a grid spacing that is much larger than individual NPs. To account for the electrostatic forces between NPs, a particle-particle algorithm was used. Particles interact through their mutual Coulombic forces shielded by the plasma. The shielded electric potential of a single NP is given by a spherically symmetric solution to the Debye Hückel equation [35],

$$\Phi(r) = \Phi_i \frac{r_i}{r}\exp\left[-\frac{(r-r_i)}{\lambda_L}\right]. \tag{7}$$

The Coulomb force between NP particles i and j at locations separated by distance $R = \left|\vec{r}_i - \vec{r}_j\right|$ is then

$$\vec{F}_{cij}(\vec{r}_i,\vec{r}_j) = \frac{Q_i Q_j}{4\pi\varepsilon_0}\frac{1}{R}\left(\frac{1}{R}+\frac{1}{\lambda_L}\right)\exp\left[-\frac{R-\left(\frac{r_i+r_j}{2}\right)}{\lambda_L}\right]\frac{\left(\vec{r}_i+\vec{r}_j\right)}{R}. \tag{8}$$

The computational time required to compute the forces between particles has poor scaling of order N^2, so only particle interactions within a few λ_L are calculated. This assumption has been found to be accurate in previous works due to the exponential decay in screening with distance [28]. Particle positions are directly compared and particles within $5\lambda_L$ of each other are saved as

pairs in arrays. These particles interact over many time steps while the list of interacting partners is only updated periodically.

The ion-drag force results from ions having a directed velocity approaching, for example, a negatively charged NP, and undergoing a parabolic (positive ion) or hyperbolic (negative ion) orbit about the NP. The change in momentum of the ion due to this orbital motion is imparted to the NP. Since the momenta of positive ions are typically directed towards the boundaries of the plasma, the ion-drag force usually accelerates NPs towards the boundaries of the plasma. In the force due to ion drag, the 4th term in Eq. 1, $\vec{\phi}_{ion}$ is the average ion momentum flux and $|\vec{v}_{ion}|$ is the mean ion speed, both obtained from the HPEM. The ion-dust momentum transfer cross section σ_{ion} is approximated using a semi-analytic equation from the work of Kilgore *et al.* [36]

$$\sigma_{ion} = b^2 c_1 \ln\left[1 + \frac{c_2}{\left(b/\lambda_L\right)^2}\right], b = \frac{Q_i^2}{4\pi\varepsilon_0\varepsilon_{ion}}. \quad (9)$$

The values of c_1=0.9369 and c_2=61.32 are semi-empirical constants from the work of Khrapak *et al.* [37], which were found to agree well with simulation and modeling results [36,38].

The forces due to viscous fluid drag (5th term in Eq. 1) are derived for hard sphere particles from classical thermodynamics [39–41]. The driving force for viscous fluid drag is the difference between the dust particle velocity ($\vec{v}_i$) and the advective fluid velocity ($\vec{u}_f$). In Eq. 1, Kn is the Knudsen number (mean free path divided by the length scale), Re_p is the particle Reynolds number, and μ is the fluid viscosity.

$$C(Kn) = 1 + Kn(\alpha + \beta)\exp\left(-\frac{\gamma}{Kn}\right), \quad (10a)$$

$$C_D(\mathrm{Re}_p)\frac{\mathrm{Re}_p}{24} = 1 + 0.173\,\mathrm{Re}_p^{0.657} + \frac{0.01721\,\mathrm{Re}_p}{1 + 16300\,\mathrm{Re}_p^{-1.09}}, \quad (10b)$$

$$\mathrm{Re}_p = \frac{2\rho r_i\left|\vec{v}_i - \vec{u}_f\right|}{\mu},. \quad (10c)$$

The constants used in Eq. 10 are listed in Table 2, where α, β, and γ are values which depend on the gas-dust surface interaction, and are measured experimentally.

The thermophoretic force (6th term in Eq. 1) results from the temperature gradient (∇T) in the gas surrounding the NP. In Eq. 1, $\nu_f = \mu/\rho_g$ is the kinematic viscosity (viscosity divided by the mass density of the gas), K_T is given by

$$K_T = \frac{2C_s\left[\left(\kappa_g/\kappa_p\right)+C_tK_n\right]}{\left(1+3C_mKn\right)\left[1+2\left(\kappa_g/\kappa_p\right)+2C_tKn\right]}, \tag{11}$$

where is κ_g is the gas thermal conductivity, κ_p is the particle thermal conductivity, and C_t, C_s, and C_m are coefficients for thermal creep, temperature jump, and velocity jumps. The values used for these constants are also in Table 2.

The last force from Eq. 1 is an effective force of Brownian motion due to random collisions with the background gas. This force is more important for smaller particles, ~1 nm where the momentum transfer from individual atoms and molecules can be significant, while decreasing in significance with increasing particle size. The magnitude of the Brownian force is

$$\left\|\vec{F}_B\right\| = \frac{M_g v_{th}\left(\pi r_i^2 \Delta t v_{th} N_g\right)^{1/2}}{\Delta t}, \quad v_{th} = \sqrt{\frac{8k_BT_g}{\pi M_g}}, \tag{12}$$

where v_{th} is the average thermal speed of the incident gas molecules (mass M_g), and Δt is the integration time step. Once the magnitude of the force is computed, the direction of the force is randomized in polar (θ) and azimuthal (ϕ) directions. The directional components of the Brownian force are then,

$$\vec{F}_{B,x} = \left\|\vec{F}_B\right\|\cos(\theta)\cos(\phi), \tag{13a}$$

$$\vec{F}_{B,y} = \left\|\vec{F}_B\right\|\cos(\theta)\sin(\phi), \tag{13b}$$

$$\vec{F}_{B,z} = \left\|\vec{F}_B\right\|\sin(\theta). \tag{13c}$$

Several new capabilities were added to the model to address growing dust particles. In previous versions of the DTS, the trajectories of non-growing particles were tracked. Here, the capability to track the mass and diameter of each dust pseudo-particle was added. The time rate of change of mass of NP *i* is given by,

$$\frac{dM_i}{dt} = \sum_j v_j N_j 4\pi r_i^2 S_{c,j}\Delta m_j, \; v_j = \sqrt{\frac{8k_BT_j}{\pi m_j}} \tag{13}$$

where the mass of dust particle *i* is M_i having radius r_i. The summation is over all the species j which contribute to dust particle growth, having thermal speed v_j, number density N_j, mass m_j and temperature T_j. The quantity Δm_j is the mass added to the dust particle which is not

necessarily equal to the incoming radical mass. The difference would account for example, the desorption of hydrogen from a sticking reaction of SiH with the dust particle. $S_{c,j}$ is the sticking probability for a collision between the dust particle and the dust growth species, which will be discussed in Section II.C.

In addition to growth by reactive species, a particle agglomeration algorithm was also added to the DTS which enables two dust particles to combine due to a collision. The algorithm tracks the distance between particle pairs. (This value is conveniently already available from the computation of Coulomb forces.) If the distance is less than the sum of the particle radii, the particles are combined into a single NP. The mass and momentum of the two combining particles are conserved in the new particle. The shape of the new particle remains a sphere with a radius given by the new mass of the combined particle and specified mass density. Since the dust particles are largely negatively charged for the conditions in this work, agglomeration is a rare occurrence.

C. Radical Sticking Probabilities

One of the most fundamental data required for modeling NP growth in a silane containing plasma is the reaction probability (or sticking coefficient) of silane radicals on the NP. These sticking coefficients were obtained using molecular dynamics simulations performed with LAMMPS [42]. $Si_{29}H_{36}$ particles were first constructed with atomic interactions modelled using a classical reactive force field [43] in combination with a dynamic charge equilibration model [44,45]. Collisions were simulated between silanes (SiH_x, x = 1-4) and the $Si_{29}H_{36}$ NP. Each $Si_{29}H_{36}$ species was prepared by generating 5 independent conformations in vacuum under canonical conditions at the target temperature (400 K) by using a stochastic velocity rescale thermostat [46]. To simulate the collisions, one of these conformations was randomly chosen and the atomic and the atomic velocities of atoms in the NP were initialized by random selection from a Maxwell-Boltzmann distribution with the additional constraint of zero linear momentum for each NP.

The SiH_x and NP were placed 2.5 nm apart (d_o) and a fixed initial speed v_i directed along the line connecting the two centers of mass was added, resulting in an impact parameter equal to zero. Speeds were chosen so that the cumulative Maxwell speed distribution was sampled uniformly at 200 intervals. The system was simulated for a for a length of time τ to satisfy $\tau \cdot v_i = 2d_o$. A total of 25 trajectories were performed for each value of v_i. The time step for

integrating trajectories was 10^{-4} fs as tests showed that longer integration times did not guarantee energy conservation during collisions.

The evolution of the system was monitored by computing the composition and the number of clusters at the end of the simulation. Two atoms were assigned to the same cluster if their distance was less than the van der Waals distance for each pair, namely 0.44, 0.32 and 0.148 nm for Si/Si, Si/H, and H/H pairs, respectively. Based on the number and composition of the clusters, the sticking probability $p(T, v_i)$ was computed at each temperature, T, and collision speed v_i. Finally, the sticking coefficient was obtained from:

$$S_c(T) = \sum_i p(T, v_i) w(T, v_i) \tag{13}$$

where the weights w are based on the Maxwell-Boltzmann distribution [47].

The resulting sticking coefficients are listed in Table 3. Generally, the probability of a silane radical to be captured by the larger particle decreases with an increase in temperature due to the average higher kinetic energy that needs to be accommodated after the collision. The number of free radical sites on the impinging silane species greatly impacts the probability of sticking. There is little likelihood of chemically bonding with 0 radical sites (SiH_4, S_c=0) for the temperatures of interest while there is nearly always sticking with 3 radical sites (SiH, S_c=0.945). The sticking probability is non-linear with free radical sites. Additional sticking coefficients were approximated for Si_2H_x species (x=2,3,5,6) based on the silane radical data and fractional number of radical sites.

III. Dust Particle Growth in Flowing Inductively Coupled Plasmas

A. Base Case

This work focuses on the consequences of electrostatic trapping on nanoparticle growth in flowing low temperature plasma reactors, as have been used in several demonstrations of plasma synthesis of nanoparticles [4,6,7,48]. An inductively coupled plasma (ICP) reactor was chosen for this work since the plasma potential is more localized and quiescent compared to capacitively coupled plasma systems. A schematic of the ICP reactor used in this computational investigation is shown in Fig. 2. For the base case, the glass tube cylindrical reactor has a radius of 1 cm and a length of 8 cm, with electrically grounded boundaries for the inlet and outlet, as would occur using a metallic mesh. Power is inductively coupled into the plasma from a three-

turn antenna delivering 10 W at 10 MHz in the base case with an inlet flow of Ar/SiH_4 = 98/2 at 50 sccm. The pressure is held constant at 1 Torr by adjusting the outlet flow rate. The temperature of the inlet gases and surrounding reactor surfaces are held constant 325 K. These operating conditions correspond to a gas residence time (τ) of 33 ms and an average energy per particle [defined as flow rate (molecules-s^{-1}) multiplied by power] of 2.8 eV, which is 0.5 eV below the average energy of breaking Si-H bonds at 3.3 eV [49].

Plasma properties for the base conditions are shown in Fig. 2. The electron density peaks close to the powered antenna at 8×10^{10} cm^{-3} and decreases by three orders of magnitude downstream by the pump. This decrease is due to the large rate of electron dissociative attachment to silane and dissociative recombination of silane ions, both of which are sources of radicals. The electron temperature T_e is maximum at 4.3 eV adjacent to the antenna, decreasing moving away from the antenna due to both elastic and inelastic collisions for the (relatively) high pressure of 1 Torr. T_e decreases to 1.5 eV downstream. Plasma potential peaks at 24.7 V off-axis (0 cm > r >1 cm) where the ion production is maximum. The surface of the dielectric tube charges negatively, down to -7.7 V at a minimum, to balance the electron and positive current to its surface. The electronegativity of the plasma is quantified by α_0, which is the ratio of the total negative ion density to the electron density. α_0 increases from 10 at the peak of the electron density to 4,000 downstream, as electrons are rapidly consumed by attachment and dissociative recombination.

The dominant positive ion at the peak of the power deposition is Ar^+ with a density of 1×10^{12} cm^{-3}, while the densities of H^+ and SiH_3^+ are more than an order of magnitude lower. The trend reverses downstream (flow distance of 7 cm) where the dominant positive ions are H^+ and SiH_3^+ with densities of 2×10^{11} cm^{-3} and 3×10^{11} cm^{-3} respectively. This change in abundance is due to the increase in density of SiH_4 fragments and their availability to charge transfer with Ar^+ whose density decays to 3×10^{7} cm^{-3} downstream. The dominant negative charge carrier throughout the reactor is $Si_2H_5^-$, with a density of 1×10^{12} cm^{-3} upstream of the power deposition zone and 5×10^{12} cm^{-3} downstream.

Gas temperature and densities of SiH_x (x=1-4) and H atoms for the base case are shown in Fig. 3. As silane flows into the reactor and encounters the region of power deposition under the antenna, electron impact dissociation depletes its density, decreasing by 2 orders of magnitude from its maximum of 4.1×10^{14} cm^{-3} by the time the flow reaches the pump.

Localized gas heating to 375 K occurs near the center of the reactor adjacent to the antenna which produces rarefaction. In addition to electron impact dissociation, dehydrogenation of SiH_x occurs progressively downstream from collisions with Ar excited states and culminates with SiH being the predominant radical. The maximum density of SiH_3 (2.0×10^{13} cm^{-3}) occurs on the upstream side of the plasma zone where SiH_4 is first dissociated. Dissociation of SiH_3 produces SiH_2 whose maximum density (1.1×10^{12} cm^{-3}) occurs near the center of the plasma zone. The maximum density of SiH (1.4×10^{12} cm^{-3}) occurs downstream of the plasma zone following dissociation of SiH_2. The H atom density has a maximum of 1.4×10^{14} cm^{-3} in the plasma zone, decreasing to less than 10^{13} cm^{-3} by the pump. In addition to reactions with silane species, H atoms also have the potential to etch the NPs and so moderate their size, a process not included in the model. This etching could impact the size of NPs that are trapped for long times.

To provide guidance on the particle growth potential of the distribution of Si_xH_y radicals, we define the reactive density N_r as the sum of the products of radical density and their sticking coefficients, S_c. The reactive density is shown in Fig. 3f. Higher densities of reactive species are found downstream, which suggests that particle growth may be important well outside the region of maximum power deposition.

Predictions from the DTS are shown in Fig. 4 for the base case conditions. The sizes of the particles are indicated by the diameter of the image's individual particles. The charge on the particles is indicated by the color of the images. 1,000 particles with a diameter of 1 nm were initialized in the reactor between the turns of the antenna. Forces acting on the particles produce negligible movement of the particles on the microsecond timescale (Fig. 4a). The currents to small particles on these time scales result in particle charging being dominated by stochastic collisions with ions and electrons, which leads to a variation in particle charges. After 0.5 ms (Fig. 4b), particles have grown on average to 1.3 nm with charges ranging from 0 to -4q with an average charge of -1.6q. For these sizes of particles and amount of charge, particle movement is dominated by electrostatic forces as particles act as large negative ions which seek the maximum in the plasma potential where they are electrostatically trapped. For these conditions, the plasma potential is maximum in an annulus centered under the antenna, which results in a torus of trapped particles. The stochastic charging process results in particles that do statistically become momentarily neutral or charged positively. Those particles that are at any time neutral tend to flow downstream due to fluid drag and thermophoretic forces, the latter which accelerates

particles away from the maximum in gas temperature under the antenna. Those particles that are momentarily charged positive are accelerated away from the maximum in plasma potential towards the walls. If not neutralized before arriving at the wall, the positively charged particles neutralize by depositing their charge on the wall.

By 4 ms (Fig. 4c), particles grow to several nm in size and become more uniform in charge with an average of -5.5q. There is still a statistical distribution of charges (-12q to 0q) though particles are almost exclusively charged negatively. Particles form a ring near the maximum in the plasma potential where the electrical forces of ion drag and electrostatic acceleration balance. After several gas residence times (τ = 33 ms, and t = 99 ms in Fig. 4d), particles grow to nearly 100 nm on the average. The position of the ring shifts further downstream as the fluid drag force increases significantly with particle size. This fluid drag then balances forces at a less positive potential in the electrostatic trap in the direction of the pump. The distribution of particle sizes and charge, and Coulomb interactions between particles prevent the particles from converging in a small volume.

Further particle growth results in fluid drag forces dominating and the particles being pulled out of the electrostatic trap. The particles then flow downstream (Fig. 4e), where the electron temperature T_e and the electron density decrease in favor of negative ions. Particle charging then becomes dominated by collisions with positive and negative ions which, downstream, have nearly equal densities and similar mobilities. These conditions reduce the need for particle charging as the floating electrical potential trends towards zero. As a result, the average particle charge also trends towards zero. In the absence of electrical forces (the ion drag, electrostatic forces and Coulomb interactions scale with particle charge), the ring of particles disperses. Growth accelerates downstream due to the higher value of N_r. By the time of exiting the reactor, particles spend nearly 4τ in the plasma by being trapped by the plasma potential. This long residence time results in fairly large particles (>100 nm).

The NP size distribution leaving the reactor is fairly mono-disperse with less than a 1% standard deviation. We attribute this narrow size distribution to the initial nuclei that are seeded in the plasma having the same size. This result implies that broad size distributions may be attributable to a random distribution of nuclei sizes.

B. Inlet SiH_4 Fraction

Lower mole fractions of SiH_4 in the inlet flow are expected to produce a more electropositive plasma while increasing silane fractions will trend towards producing an ion-ion plasma. The consequences of inlet silane mole fraction (0.1% to 50%) on electron density, plasma potential, SiH_4 density and N_r are shown in Figs. 5 and 6. Other parameters from the base conditions were held constant – 1 Torr, 10 W at 10 MHz, with 50 sccm total inlet flow. Values in Figs. 5 and 6 are shown as a function of axial position (measured from the inlet) on the axis of the reactor (r = 0 cm). The electron density increases with decreasing SiH_4 inlet fraction due to lower rates of power loss to non-ionizing collisions (dominantly dissociation of SiH_x) and lower rates of electron attachment to form negative ions. In all cases, the electron density decreases by at a factor of at least 10^4 due to the presence of thermally attaching Si_xH_y radicals and dissociative recombination. At lower SiH_4 fractions (< 2%), the dominant ion shifts from SiH_3^+ to Ar^+ even in the region of the maximum power deposition. Increasing the SiH_4 mole fraction leads to flatter axial profiles in the plasma potential resulting from the lower electron density and increased electronegativity, while there is an increasingly higher plasma density and potential off-axis due to more localized power deposition.

The fractional dissociation of SiH_4 increases with decreasing inlet mole fraction. Decreasing inlet SiH_4 fraction results in increased gas heating. An increase in T_e produces an increase in plasma potential which in turn produces more ion acceleration leading to charge exchange heating. The higher gas temperature leads to more rarefaction. The weighted densities of reactive species N_r, shown in Fig. 6b, increase with increasing inlet fraction, which should lead to faster particle growth. There is only a small difference in N_r when increasing the inlet mole fraction from 25% to 50%. By this mole fraction, the production of radicals is limited by power deposition and not by availability of silane.

The average particle diameters as a function of time for different silane mole fractions are shown in Fig. 6c. The particle growth rates increase with increasing SiH_4 inlet fraction due to the increase in N_r. Particle sizes are shown up to the time that the (untrapped) particles flow out of the reactor. Particles for the two lowest fractions of SiH_4 (0.1% and 0.25%) remain trapped in the plasma over the total simulation time (500 ms, >10 τ) and do not flow out of the reactor. The final particle sizes do not directly correspond with growth rates. For example, the final particles sizes are 26.7, 62.7, 42.7, and 86.8 nm for 0.1, 0.25, 0.5 and 1.0% SiH_4 fractions. The final

particle size results from the integrated growth during the particle's entire residence time in the reactor. The particle's residence time is determined by the trapping electrical potential in the plasma (larger for smaller mole fractions) and the densities of growth species (larger for larger mole fractions). Increasing particle size increases the fluid drag forces, while the electrostatic force depends on particle charge and the local electric field. Therefore, particles reach the critical size which enables fluid drag forces to overcome the trapping potential and flow out of the reactor at different sizes for different silane mole fractions. Once the NPs escape from the electrostatic trap, they continue to grow while flowing downstream through regions where N_r is large.

For example, the gas residence time is τ=33 ms in these cases based solely on flow rate and volume of the reactor. Accounting for differences in position of the maximum in plasma potential, the NPs particles should flow out of the reactor in ≈20 ms after reaching a critical size where fluid drag overcomes the electrostatic force. For the base conditions (2% SiH_4), particles should take about 100 ms to reach this size as shown in Fig. 4c. The time that the particles flow out of the reactor is 120 ms, as shown in Fig. 6c). Decreasing the inlet SiH_4 fraction increases the trapping potential while the growth rate decreases. The balance of residence vs growth rate favors the influence of growth rate, which overall results in smaller particles.

Increasing the inlet SiH_4 fraction results in a mix of smaller, similarly sized, and a few larger particles due to the decreased trapping potential but highly increased growth rates. The highest inlet fractions have a nearly flat axial plasma potential having only moderate trapping which results in particles flowing out of the plasma in approximately one residence time. This shorter exposure time to radicals then decreases the final particle size. However, a few ms of extra time trapped in the plasma can lead to significantly larger particles. For example, the particle size increases from 126 nm to 153 nm in going from 50% to 25% inlet SiH_4 fraction, the latter having a more positive trapping potential, while the density of growth species N_r is nearly the same. With particles trapped for 5.0 ms longer for the smaller mole fraction, overall growth is proportionately larger.

Overall, the growth rates of particles in the plasma closely follow from what one might expect intuitively – increased inlet mole fraction produces larger densities of growth precursor which enables higher growth rates. However, the final particle sizes are ultimately determined by residence times of particles in the presence of the growth species, which in turn are

determined by the trapping of negatively charged NPs in the plasma.

C. Gas Residence Time (τ)

Negatively charged NPs can remain in the plasma for several gas residence times due to electrostatic trapping, while the total time spent in the plasma directly impacts the size of the NPs. The impact of gas residence time (τ) was investigated by performing simulations with τ in the range of 10 ms to 500 ms. The specific input parameters are listed in Table 4 in the Appendix. With constant power deposition, residence time determines the energy deposition per inlet molecule which then affects fractional dissociation and radical production. To minimize these dependencies the power deposition was adjusted (0.67 W to 33.3 W) to produce a constant energy deposition per inlet molecule/atom of 2.8 eV. Higher powers are applied to higher flow rates to maintain the constant specific energy deposition.

Plasma properties for different gas residence times are shown in Fig. 7 as a function of axial distance from the inlet on axis (r = 0). Electron densities increase with decreasing residence time (higher flow rate) due to the higher applied power required to keep the energy deposition per molecule constant. The electron temperature has a consistent profile for all cases with a slight trend for increasing temperature with increasing gas residence time. With the gas mole fractions, dissociation fraction and gas temperatures nearly the same (due to the constant energy deposition/molecule), the self-sustaining electron temperature is also nearly the same. Since the plasma potential in glow discharges generally scales with electron temperature, the plasma potential has nearly the same peak value between the turns of the antenna, while the profile becomes more uniform along the reactor length with increasing τ (lower flow rate). This is indicative of transitioning from an electropositive to an electronegative plasma with increasing gas residence time.

The densities of particle growth species are shown in Fig. 8. Longer gas residence times τ (lower flow rates) result in diffusive transport being more dominant, producing more uniform distributions of SiH_4 and reactive dissociation products. With shorter residence times τ (higher flow rates) advective transport dominates with there being less opportunity for diffusion upstream towards the inlet. As a result, the reactive density N_r, for τ = 10 ms is negligible at the inlet with there being larger densities downstream. Conversely with τ = 500 ms, the diffusion of reactants upstream is able to compete with advection downstream, and the distribution of N_r is

nearly uniform. However, when integrating along the length of the discharge, the average value of N_r is nearly constant since the energy deposition per molecule is constant.

Particle diameters as a function of time for different flow rates (growth rates being the slope of diameter vs time) are shown in Fig. 8c. Increasing the gas residence time increases the final particle size. The fluid drag force scales with fluid velocity which decreases with longer gas residence times (lower flow rates). The end result is that similarly sized and charged particles are trapped at the peak of the plasma potential (similar for all flow rates) longer for lower flow rates (long τ). Particle growth rates increase for shorter residence times due to there being higher densities of reactive species at the location of the particle trap at the peak in plasma potential at ≈2.5 cm. However, with the higher flow rates, the particles stay trapped for a shorter period of time, which reduces their final size.

D. Energy Deposition Per Particle

Power deposition is one of the primary control parameters for particle growth as power directly impacts the densities of reactive species. However, the inventory of reactive species is determined by the fractional dissociation of the feedstock SiH_4, which in turn is largely determined by the energy deposition per inlet molecule (E_p). However, even when controlling for E_p, electron density and gas heating can impact particle growth rates and so the final particle size. A parameterization of energy per particle E_p was conducted while varying power from 0.5 W to 25 W, producing values of E_p of 0.14 to 7.0 eV/particle. The range of conditions are shown in Table 5 of the Appendix.

The electron density and plasma potential as a function of distance from the inlet on axis (r = 0) for different energy per particle (E_p) are shown in Fig. 9 for otherwise the base-case conditions. The peak electron density spans 2 orders of magnitude from the lowest power (0.5 W, $n_e \approx 2\times10^9$ cm^{-3}, E_p = 0.14 eV/particle) to the highest power (25 W, $n_e \approx 3\times10^{11}$ cm^{-3}, E_p = 7.0 eV/particle). The majority of this increase is simply due to the 50-fold increase in power deposition. Other contributions include the increasing dissociation of SiH_4 and increasing gas temperature, both of which make for less collisional conditions and higher ionization efficiency. The maximum gas temperature spans 327 to 465 K for 0.5 W to 25 W. The electron density decreases downstream in all cases due to thermal attachment to radicals, dissociative recombination and diffusion to the walls.

Axial profiles for silane fraction are shown in Fig. 10a and reflect the increasing rates of

dissociation and rarefaction with increasing power. With only 2.5 W (E_p = 0.70 eV/particle), the SiH_4 fraction decreases to less than 10% that at the inlet. For higher powers, the dissociation of SiH_4 is nearly complete. However, the fractional decrease is in part exaggerated by the increase in the total density due to the production of dissociation fragments. The rebound in silane mole fraction downstream can be largely attributed to H atom consumption. For low powers (0.5 W, E_p = 0.14 eV/particle and 1 W, E_p = 0.28 eV/particle), the fractional dissociation of SiH_4 is smaller and the fraction of H atoms is an order of magnitude (or more) smaller than SiH_4. For higher power, the dissociation of SiH_4 is nearly complete which leads to H fractions exceeding those of SiH_4 under the antenna. At 25 W (E_p = 7.0 eV/particle), the SiH_4 fraction is 2 orders of magnitude smaller than that of H atoms (0.004% compared to 0.8%). Once formed, H radicals are reactive and recombine on the walls, decreasing their density downstream, leaving the reactor with a mole fraction of 0.02%. The end result is an increase in the SiH_4 mole fraction to 0.01% at the pump.

The densities of the weighted growth species, N_r, are shown in Fig. 10b for different E_p. The general trend is as expected – N_r increases with increasing power. At powers above 10 W (E_p = 2.8 eV/particle), the silane is highly dissociated and N_r begins to saturate. Even with the silane fully dissociated, N_r continues to increase as, for example, SiH_3 is converted to SiH_2 which has a higher sticking probability and so a larger contribution to N_r.

Average NP sizes as a function of time for different E_p are shown in Fig. 10c. As expected, the particle growth rate (slope of the size vs time) increases with increasing E_p due to the increase in reactive species densities. The time that a particle spends in the plasma increases up to an energy deposition of E_p = 4.2 eV/particle or 15 W. (Recall that the data in Fig. 10c extends to when the particles leave the system if not trapped.). Lower E_p produces smaller local maxima in the plasma potential with lower electron densities. The confining electric fields are smaller and there is less particle charging. As a result, fluid drag forces overcome the electrostatic trapping forces at smaller NP size, which reduces residence time and particle size. For E_p > 4.2 eV/particle (power > 15 W), the particles grow faster due to the increase in N_r however the trapping potential is also lower, enabling fluid drag to overcome the trapping potential earlier. This shorter residence time leads to final particle sizes decreasing for higher powers. Even with faster growth rates, if the particles are trapped for less time the net growth can be less.

E. Gas Pressure

Nanoparticles are typically grown in plasmas having pressures of half to a few Torr. However even within this range of pressure, discharge characteristics can vary significantly. The consequences of gas pressure on NP growth for a pressure range of 0.25 to 2.5 Torr were investigated, with the input parameters shown in Table 6 of the Appendix. The parameters were chosen to have a constant gas residence time and constant energy per particle. Axial profiles for plasma properties while varying gas pressure are shown in Fig. 11. The inventory of electrons (volume integral of plasma density) is fairly constant as the energy/particle is constant. The peak electron density increases with increasing pressure at the location of maximum power deposition due to the decrease in electron mean free path (0.34 cm to 0.03 cm from 0.25 to 2.5 Torr at 325 K) while the downstream electron density decreases with increasing pressure. Higher pressures increase the rate of electron energy loss, thereby confining the region of net positive ionization to the vicinity of the antenna. The on-axis electron temperature decreases with increasing pressure at the location of maximum power deposition due to lower rates of diffusion loss. Plasma potential decreases in magnitude with increasing pressure due to this lower electron temperature and an increase in electronegativity.

Axial profiles of silane mole fraction and N_r for different pressures are shown in Fig. 12 as a function of distance from the inlet. The upstream SiH_4 fraction increases with increasing pressure as bulk fluid flow begins to dominate over diffusion – there is less of a spatial averaging of the depletion of SiH_4 at higher pressures. Downstream the trend is the opposite with decreasing silane mole fraction for higher pressures. With the decrease in importance of axial diffusion with increasing pressure, advection dominates the transport of silane.

The weighted growth species density N_r, as shown in Fig. 12b, increases with increasing pressure due, in part, to lower diffusion loses. Average particle diameters as a function of time for different pressures are shown in Fig. 12c. The particle growth rate increases with increasing pressure due to the increase in the densities of growth species. Particles are trapped in the plasma for longer periods with decreasing pressure due to the lower fluid drag forces and larger plasma potential. At the lowest pressures (0.5 and 0.25 Torr), the particles remained in the reactor until the end of the simulation time (500 ms). For the higher pressures typically used to grow particles, the final particle sizes range between 100 – 120 nm. These trends may indicate that pressure is not a major factor in determining particle size (keeping other parameters

constant), and could instead be used to fine-tune the gas residence time and eV/particle.

F. Radius of Plasma Tube

A large portion of experimental work on plasma synthesis of nanoparticles has been performed using cylindrical (glass tube) reactors. As there has been little standardization of reactor specifications, the consequences of reactor dimensions on particle growth were investigated. The tube radius was varied while keeping the gas residence time, pressure and energy per particle constant. Achieving these constraints requires adjusting both the input power and the inlet flow rate. The parameters varied in this study are in Table 7 of the Appendix.

The radius of the plasma tube was varied from 0.75 to 1.5 cm while keeping the reactor length 8 cm. The resulting axial profiles of plasma properties are shown in Fig. 13. With constant energy deposition per particle, the maximum plasma density is nearly constant with a maximum occurring off axis near the antenna from 7.2×10^{10} cm^{-3} to 1.0×10^{11} cm^{-3} for 0.75 and 1.5 cm radius respectively. The larger rate of radial diffusion with smaller radii produces a larger decrease in electron density with flow downstream. In a classical glow discharge with electron losses dominated by diffusion to the walls, electron temperature increases with decreasing radius to increase ionization to offset these losses. Since electron losses in the region of maximum power is a mix of attachment, dissociative recombination and diffusion, the electron temperature only modestly increases on axis (3.3 eV to 3.6 eV) with decreasing radius while a radius decrease from 1.5 cm to 0.75 cm increases diffusion losses by a factor of 4. Near the antenna, the electron temperature is 4.2 to 4.3 eV for all reactor radii. For nearly constant plasma density and pressure, the electromagnetic skin depth is nearly constant (≈1.9 cm) and so power deposition occurs closer to the axis with smaller tubes. This increase in local power deposition then contributes to the increase in T_e along the axis. The peak plasma potential relative to the negative wall potential is nearly constant as a function of radius of the discharge tube, having a small increase due to the increase in electron temperature. Here, the plasma potential relative to ground decreases with increasing radius due to negative charging of the glass tube.

Silane mole fraction and reactive species density N_r for different radii are shown in Fig. 14. With residence time, energy per particle and pressure constant, the profiles of silane density are similar. The lower silane mole fraction for smaller radius is attributable to the electromagnetic skin depth reaching to the axis with there being more power deposition adjacent

to the axis. (In a perfectly cylindrically symmetric system with purely collisional power deposition, the inductively coupled power on the axis is zero.). In spite of maintaining energy per particle constant, there is an increasing density of particle growth species with increasing radius, likely a result of more wall losses by diffusion at small radii. The increase in N_r leads to a higher rate of particle growth for larger radii, as shown in Fig. 14c. The electrostatic plasma potential traps NP in a ring near the peak plasma potential adjacent to the powered antenna where the plasma properties are a weak function of radii. Particles reach similar sizes before fluid drag dominates, which results in particles with a final size of ≈120 nm.

IV. Concluding Remarks

The trapping of nanoparticles (NP) in low temperature plasmas largely results from their acquiring negative charge and being attracted to the maximum in plasma potential. In ICPs, this maximum occurs in the vicinity of the antenna. In flowing reactors, the final NP size results from the residence time of the NP and the local density of radicals which contribute to its growth. The location of electrostatic trapping of NPs will depend on other forces (e.g., particle-particle Coulomb interactions, ion-drag, thermophoresis). However, these forces in ICPs are typically not large enough to remove NPs from the trap. In flowing plasmas, the particles are generally removed from the trap by fluid drag when reaching a critical size. Results from a computational investigation were discussed to develop scaling laws for the growth of Si nanoparticles in ICPs based on their trapping and ultimately de-trapping.

The growth rates and final sizes of NPs can be controlled by tuning the gas residence time and energy deposition per particle. Small nanometer sized particles charge primarily negative and are most sensitive (on a relative basis compared to other forces) to the electrostatic positive plasma potential. This electrostatic trapping enables small particles to remain in the reactor for times exceeding several gas residence times - growing until a critical threshold in size is reached where fluid drag becomes a dominant force to remove the particles from the trap. Once the NPs are entrained in the gas flow, they generally enter a region downstream in which the density of growth species is larger, thereby enhancing their growth rates. The final particle size is then determined by two residence times – the time the particle spends in the electrostatic trap and the time the particle spends flowing downstream through the higher density of growth species, a fraction of the gas residence time.

The inlet fraction of precursor gas, silane in this study, directly affects the growth rates of the nanoparticles due to increased availability of growth species. However, large SiH_4 fractions create electronegative plasmas in which the trapping potential for negative charged NPs can be significantly lower. This lower trapping potential reduces the residence time of NPs in the electrostatic trap, which leads to some unpredictability in final particle sizes.

When keeping energy deposition per particle constant, gas residence time can be used to control final particle size. Longer residence times (lower flow rates) result in lower growth rates due to there being lower local densities of growth species whose transport is dominated by diffusion rather than advection. However, final particle size increases with increasing gas residence time (lower flow rates) due to the NPs spending much more time in the plasma. NPs must reach a size where fluid drag can overcome the electrostatic trapping potential and then flow out of the reactor over the gas residence time while continually growing.

Energy per particle E_P directly affects the densities of reactive species and so the growth rates of nanoparticles. With increasing E_P (or power for all other parameters remaining constant), production of growth species eventually saturates due to dissociation of the feedstock gases. Power also to some degree controls the trapping potential for NPs as increasing power decreases the electronegativity of the plasma and increases rarefaction. It was found that these competing factors leave room for optimization – for a given set of operating conditions, there may be an optimum power or E_P to produce a given size particle.

When controlling for gas residence time and E_P, nanoparticles grow faster at higher pressure due to there being higher densities of reactive growth species. However, final particle size remained similar across a range of pressures (0.75 to 2.5 Torr) due to there being increased fluid drag and lower trapping potential at higher pressure which ultimately reduces the residence time of the NPs. Gas pressure may also be a tuning parameter when the goal is to keep the NP size constant while varying other properties (e.g., core-shell particles).

The choice of LTP reactor to synthesize NPs having desired morphological or compositional properties is a multi-dimensional optimization process. Current best practice has evolved to use capacitively coupled plasmas (CCPs) [50]. The growth of NPs in these systems has been robust and able to synthesize a variety of types of NPs [5,51,52]. The plasma potential in these CCPs, at least in the tubular reactors now commonly used to synthesize NPs, is less well defined spatially, which leads to difficulty in controlling the electrostatic trapping potential that

enables predictable and controlled growth of NPs. With the plasma potential more localized and predictable in ICPs, avenues open up to use the electric trap as an incubator for particle growth, which is then emptied when the NPs reach a critical size. This capability, perhaps combined with power pulsing, would provide an avenue to finely control the size of NPs in the range of 20-100 nm. This advantage diminishes for NPs of less than a few nm in size when the stochastic charging of the particles may produce a distribution of negative, positive and neutral NPs. The positive and neutral NPs are less controllable due to their inability to be trapped.

In addition to control of the size and properties of the NPs, utilization of the feedstock gases, silane in this case, is also important in industrial applications. Ultimately the rate of production of NPs and cost (in part determined by utilization of feedstock gases) determine the practicality of industrially implementing these techniques. Since ICPs typically produce larger dissociation fractions than CCPs for otherwise identical operating conditions, the average radical has a higher sticking coefficient in ICPs compared to CCPs. These higher sticking coefficients are beneficial with respect to NP nucleation and growth. However, the higher sticking coefficients are detrimental with respect to sticking to and film growth on walls, which is loss reducing feedstock utilization. In this regard, control of wall conditions (e.g., temperature) may be important in reducing film growth and increasing utilization. Here, CCPs may have an advantage over ICPs in that the average ion energy striking surfaces is higher in CCPs than ICPs. These higher ion energies produce higher rates of sputtering of films on the walls, at least those in the active plasma zone, returning SiH_x radicals to the gas phase which can participate in particle growth. An optimized process that takes advantage of the controlled trapping afforded by ICPs while limiting film growth and increasing utilization might use an ICP operating in a mixed E-mode and H-mode [54]. The mixed E-mode/H-mode operation will produce more energetic ions onto surfaces to sputter film while not significantly perturbing the cycle averaged plasma potential.

Data Availability

The processed data that supports our conclusions are contained in this article. The raw data resulting from the simulations are available upon reasonable request.

Acknowledgements

The authors thank Profs. Uwe Kortshagen and Elijah Thimsen for their insights during discussion of these results. This work was supported by Army Research Office MURI Grant W911NF-18-1-0240, the National Science Foundation (IIP-1747739, PHY-2009219) and the Department of Energy Office of Fusion Energy Science (DE-SC0020232).

References

[1] U. Kortshagen, J. Phys. D. Appl. Phys. **42,** (2009).

[2] A. Bapat, C. Anderson, C. R. Perrey, C. B. Carter, S. A. Campbell and U. Kortshagen, Plasma Phys. Control. Fusion **46,** (2004).

[3] U. Kortshagen, Plasma Chem. Plasma Process. **36,** 73 (2016).

[4] L. Mangolini, E. Thimsen and U. Kortshagen, Nano Lett. **5,** 655 (2005).

[5] A. Alvarez Barragan, N. V. Ilawe, L. Zhong, B. M. Wong and L. Mangolini, J. Phys. Chem. C **121,** 2316 (2017).

[6] E. Thimsen, U. R. Kortshagen and E. S. Aydil, J. Phys. D. Appl. Phys. **48,** (2015).

[7] B. L. Greenberg, S. Ganguly, J. T. Held, N. J. Kramer, K. A. Mkhoyan, E. S. Aydil and U. R. Kortshagen, Nano Lett. **15,** 8162 (2015).

[8] A. Ho, R. Mandal, R. R. Lunt and R. J. Anthony, ACS Appl. Nano Mater. **4,** 5624 (2021).

[9] C. R. Gorla, S. Liang, G. S. Tompa, W. E. Mayo and Y. Lu, J. Vac. Sci. Technol. A Vacuum, Surfaces, Film. **15,** 860 (1997).

[10] U. R. Kortshagen, R. M. Sankaran, R. N. Pereira, S. L. Girshick, J. J. Wu and E. S. Aydil, Chemical Reviews **116,** 11061 (2016).

[11] A. Izadi and R. J. Anthony, Plasma Process. Polym. **16,** 1 (2019).

[12] L. Boufendi and A. Bouchoule, Plasma Sources Sci. Technol. **3,** 262 (1994).

[13] V. A. Schweigert and I. V. Schweigert, J. Phys. D. Appl. Phys. **29,** 655 (1996).

[14] P. Agarwal and S. L. Girshick, Plasma Sources Sci. Technol. **21,** (2012).

[15] C. Cui and J. Goree, IEEE Trans. Plasma Sci. **22,** 151 (1994).

[16] P. Agarwal and S. L. Girshick, Plasma Chem. Plasma Process. **34,** 489 (2014).

[17] U. Kortshagen and U. Bhandarkar, Phys. Rev. E - Stat. Physics, Plasmas, Fluids, Relat. Interdiscip. Top. **60,** 887 (1999).

[18] R. Le Picard, A. H. Markosyan, D. H. Porter, S. L. Girshick and M. J. Kushner, Plasma Chem. Plasma Process. **36,** 941 (2016).

[19] X. Chen and C. J. Hogan, Chem. Eng. J. **411,** 128383 (2021).

[20] M. J. Kushner, J. Phys. D. Appl. Phys. **42,** 194013 (2009).

[21] M. J. Kushner, J. Appl. Phys. **71,** 4173 (1992).

[22] J. Perrin, O. Leroy and M. C. Bordage, Contrib. to Plasma Phys. **36,** 3 (1996).

[23] C. K. Goertz, Rev. Geophys. **27,** 271 (1989).

[24] O. Havnes, T. K. Aanesen and F. Melandsø, J. Geophys. Res. **95,** 6581 (1990).

[25] J. Goree, Plasma Sources Sci. Technol. **3,** 400 (1994).

[26] R. N. Franklin, Plasma Sources Sci. Technol. **11,** (2002).

[27] H. H. Hwang, E. R. Keiter and M. J. Kushner, J. Vac. Sci. Technol. A Vacuum, Surfaces, Film. **16,** 2454 (1998).

[28] V. Vyas, G. A. Hebner and M. J. Kushner, J. Appl. Phys. **92,** 6451 (2002).

[29] S. J. Choi, P. L. G. Ventzek, R. J. Hoekstra and M. J. Kushner, Plasma Sources Sci. Technol. **3,** 418 (1994).

[30] J. E. Allen, Phys. Scr. **45,** 497 (1992).

[31] J. E. Allen, B. M. Annaratone and U. De Angelis, J. Plasma Phys. **63,** 299 (2000).

[32] A. A. C. Atkinson, S. Journal, R. Statistical, S. Series and C. A. Statistics, J. R. Stat. Soc. Ser. C (Applied Stat. **28,** 29 (1979).

[33] J. E. Daugherty, R. K. Porteous, M. D. Kilgore and D. B. Graves, J. Appl. Phys. **72,** 3934 (1992).

[34] M. Gatti and U. Korshagen, Phys. Rev. E **78**, 046402 (2008).

[35] J. E. Daugherty, R. K. Porteous and D. B. Graves, J. Appl. Phys. **73,** 1617 (1993).

[36] M. D. Kilgore, J. E. Daugherty, R. K. Porteous and D. B. Graves, J. Appl. Phys. **73,** 7195 (1993).

[37] S. A. Khrapak, A. V. Ivlev, G. E. Morfill and H. M. Thomas, Phys. Rev. E - Stat. Physics, Plasmas, Fluids, Relat. Interdiscip. Top. **66,** 4 (2002).

[38] S. J. Choi and M. J. Kushner, IEEE Trans. Plasma Sci. **22,** 138 (1994).

[39] L. Talbot, R. K. Cheng, R. W. Schefer and D. R. Willis, J. Fluid Mech. **101,** 737 (1980).

[40] G. K. Batchelor and C. Shen, J. Colloid Interface Sci. **107,** 21 (1985).

[41] D. J. Rader and A. S. Geller, Plasma Sources Sci. Technol. **3,** 426 (1994).

[42] S. Plimpton, Journal of Computational Physics **117,** 1 (1995).

[43] J. C. Fogarty, H. M. Aktulga, A. Y. Grama, A. C. T. Van Duin and S. A. Pandit, J. Chem. Phys. **132,** (2010).

[44] N. Aiichiro, Comput. Phys. Commun. **104,** 59 (1997).

[45] A. K. Rappé and W. A. Goddard, J. Phys. Chem. **95,** 3358 (1991).

[46] G. Bussi, D. Donadio and M. Parrinello, J. Chem. Phys. **126,** (2007).

[47] X. and E. Shi Paolo and Violi, Angela, J. Phys. D. Appl. Phys. (2021).

[48] K. I. Hunter, J. T. Held, K. A. Mkhoyan and U. R. Kortshagen, ACS Appl. Mater. Interfaces **9,** 8263 (2017).

[49] In Encyclopedia of Inorganic Chemistry (American Cancer Society, 2006).

[50] X. Chen, T. Seto, U. R. Kortshagen and C. J. Hogan, Powder Technol. **373,** 164 (2020).

[51] S. Exarhos, A. Alvarez-Barragan, E. Aytan, A. A. Balandin and L. Mangolini, ACS Energy Lett. **3,** 2349 (2018).

[52] A. Woodard, K. Shojaei, G. Nava and L. Mangolini, Plasma Chem. Plasma Process. **38,** 683 (2018).

[53] R. C. Weast, D. R. Lide, M. J. Astle and W. H. Beyer, *CRC Handbook of chemistry and physics*, CRC Press (1989).

[54] C. Qu, S. J. Lanham, S. C. Shannon, S. K. Nam and M. J. Kushner, J. Appl. Phys. **127**, 133302 (2020).

Figure Captions

1. Particle charging charactertistics. a) Particle charge (in units of elementary charge) as a function of particle size (1 – 100 nm) for particles immersed in the base case reactor (1 Torr, 10 W, 50 sccm, Ar/SiH_4 = 98/2). The particles were initialized in the same position in the reactor with no movement to isolate the charging algorithm. b) Standard deviation of the charge fluctuations scaled by the mean particle charge for particle sizes of 1 – 100 nm. The magnitude of the relative charge fluctuations decrease with increasing particle size.
2. Reactor and plasma properties for the base case conditions (1 Torr, 10 W, 50 sccm, Ar/SiH_4 = 98/2). a) Schematic of the reactor, b) electron density, c) electron temperature, d) electric potential and e) electronegativity parameter $\alpha = [N^-]/[e]$. The maximum value is shown in each frame. *2 dec* or *3 dec* indicates the number of decades plotted on a log-scale.
3. Plasma properties for the base case conditions (1 Torr, 10 W, 50 sccm, Ar/SiH_4 = 98/2). a) Gas temperature (T_{gas}), b) SiH_4 density, c) SiH_3 density, d) SiH_2 density, e) SiH density, f) H density and g) N_r (sum of radical density times sticking coefficient to the NP). The maximum value is shown in each frame. *2 dec* or *3 dec* indicates the number of decades plotted on a log-scale.
4. Particle locations for the base case conditions (1 Torr, 10 W, 50 sccm, Ar/SiH_4 = 98/2) at different times a) 0.8 μs, b) 0.4 ms, c) 4.3 ms, d) 99 ms and e) 116 ms. The sizes of the NPs are indicated by the size of the individual images. The charge on the NPs are color coded, with the range of charge noted in each frame.
5. Plasma properties along the axis while varying SiH_4 inlet fraction from 0.1% to 50%. a) Electron density and b) plasma potential. Curves are labeled with the SiH_4 mole fraction.
6. Plasma and particle properties along the axis while varying SiH_4 inlet fraction from 0.1% to 50%. a) SiH_4 mole fraction, b) density of scaled growth species, N_r and c) average particle sizes as a function of time. Curves are labeled with the SiH_4 mole fraction.
7. Plasma properties along the axis while varying gas residence time from 10 ms to 500 ms. a) Electron density, b) electron temperature and c) plasma potential. Curves are labeled with the gas residence time.
8. Plasma and particle properties along the axis while varying gas residence time from 10 ms to 500 ms. a) SiH_4 mole fraction, b) density of scaled growth species, N_r and c) average particle sizes as a function of time. Curves are labeled with the gas residence time.

9. Plasma properties along the axis while varying energy/particle E_P from 0.14 to 7.0. a) Electron density and b) plasma potential. Curves are labeled with the value of E_P.
10. Plasma and particle properties along the axis while varying energy/particle E_P from 0.14 to 7.0 eV/particle. a) SiH_4 mole fraction, b) density of scaled growth species, N_r and c) average particle sizes as a function of time. Curves are labeled with values of E_P.
11. Plasma properties along the axis while varying gas pressure for 0.25 to 2.5 Torr. a) Electron density, b) electron temperature and c) plasma potential. Curves are labeled with the gas pressure.
12. Plasma and particle properties along the axis while varying gas pressure from 0.25 to 2.5 Torr. a) SiH_4 mole fraction, b) density of scaled growth species, N_r and c) average particle sizes as a function of time. Curves are labeled with the gas residence time.
13. Plasma properties along the axis while varying radius of the discharge tube from 0.75 to 1.5 cm. a) Electron density, b) electron temperature and c) plasma potential. Curves are labeled with the tube radius.
14. Plasma and particle properties along the axis while varying radius of the discharge tube from 0.75 to 1.5 cm. a) SiH_4 mole fraction, b) density of scaled growth species, N_r and c) average particle sizes as a function of time. Curves are labeled with the tube radius.

Table 1. Species Used in the Plasma Chemistry Model.

Argon and electrons

Ar, Ar($1s_5$), Ar($1s_4$), Ar($1s_3$), Ar($1s_2$), Ar(4p), Ar(4d), Ar^+, e

Hydrogen species

H_2, H_2^*, H, H^*, H^+

Silane species

SiH_4, SiH_3, SiH_2, SiH, Si_2H_6, Si_2H_5, Si_2H_3, Si_2H_2, SiH_3^+, SiH_3, SiH_2^-

Table 2. Constants Used in Calculation of Fluid Drag and Thermophoresis Forces.

Constant	Value	Reference
α	1.227	[40]
β	0.42	[40]
γ	0.85	[40]
C_t	2.20	[39,40]
C_s	1.147	[39,40]
C_m	1.146	[39,40]
k_g	0.1799 $mWcm^{-1}K^{-1}$	[52]
k_p	1240 $mWcm^{-1}K^{-1}$	[52]

Table 3. Species sticking coefficients (S_c) onto NPs used in this work derived using molecular dynamics simulation. The technique consists of launching molecules onto a representative $Si_{29}H_{36}$ molecule and counting the fraction of chemisorbed impacts. Note that the coefficients for Si_2H_x species were estimated based on the number of dangling bonds with reference to SiH_x values.

Species	S_c	T_{gas}
SiH_4	0.	400
SiH_3	0.125	400
SiH_2	0.66	400
SiH	0.945	400
Si_2H_6	0.	
Si_2H_5	0.1	
Si_2H_3	0.3	
Si_2H_2	0.66	

Appendix

Table 4. Operating conditions for the parameter sweep varying input gas flow rate to control gas residence time (τ). Input silane fraction remained at 2%.

Pressure (Torr)	Flow rate (sccm)	Power (W)	τ (ms)	Energy per particle (eV)
1	167.8	33.4	10	2.8
1	66.7	13.3	25	2.8
1	50.0	10	33	2.8
1	41.7	8.3	40	2.8
1	33.4	6.7	50	2.8
1	22.2	4.4	75	2.8
1	16.7	3.3	100	2.8
1	11.1	2.2	150	2.8
1	8.3	1.7	200	2.8
1	6.7	1.3	250	2.8
1	3.3	0.67	500	2.8

Table 5. Operating conditions for the parameter sweep varying energy per particle. The input fraction of SiH_4 remains at 2%.

Pressure (Torr)	Flow rate (sccm)	Power (W)	τ (ms)	Energy per particle (eV)
1	50	0.5	33	0.14
1	50	1.0	33	0.28
1	50	2.5	33	0.70
1	50	5.0	33	1.4
1	50	10	33	2.8
1	50	15	33	4.2
1	50	20	33	5.6
1	50	25	33	7.0

Table 6. Operating conditions for the parameter sweep varying gas pressure, keeping gas residence time and energy per particle constant.

Pressure (Torr)	Flow rate (sccm)	Power (W)	τ (ms)	Energy per particle (eV)
0.25	12.5	2.5	33	2.8
0.5	25	5	33	2.8
0.75	37.5	7.5	33	2.8
1.0	50	10	33	2.8
1.25	62.5	12.5	33	2.8
1.5	75	15	33	2.8
1.75	87.5	17.5	33	2.8
2.0	100	20	33	2.8
2.5	125	25	33	2.8

Table 7. Operating conditions for the parameter sweep varying radius of the discharge tube while keeping gas residence time, energy per particle and inlet silane mole fraction constant 2%.

Radius (cm)	Length (cm)	Pressure (Torr)	Flow rate (sccm)	Power (W)	τ (ms)	Energy per particle (eV)
0.75	8	1.0	28.1	5.6	33	2.8
1.0	8	1.0	50	10.0	33	2.8
1.25	8	1.0	78.1	15.6	33	2.8
1.5	8	1.0	112.5	22.5	33	2.8

AIP Publishing

Journal of Applied Physics

ACCEPTED MANUSCRIPT

PLEASE CITE THIS ARTICLE AS DOI: 10.1063/5.0062255

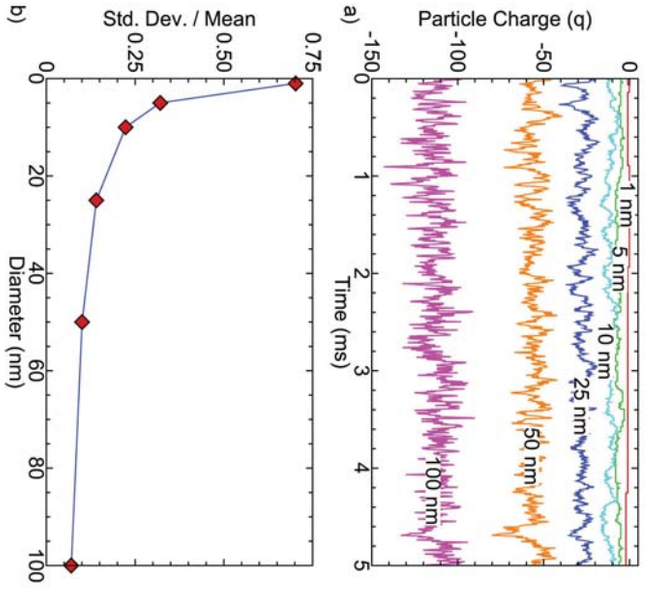

AIP Publishing

Journal of Applied Physics

ACCEPTED MANUSCRIPT

This is the author's peer reviewed, accepted manuscript. However, the online version of record will be different from this version once it has been copyedited and typeset.
PLEASE CITE THIS ARTICLE AS DOI: 10.1063/5.0062255

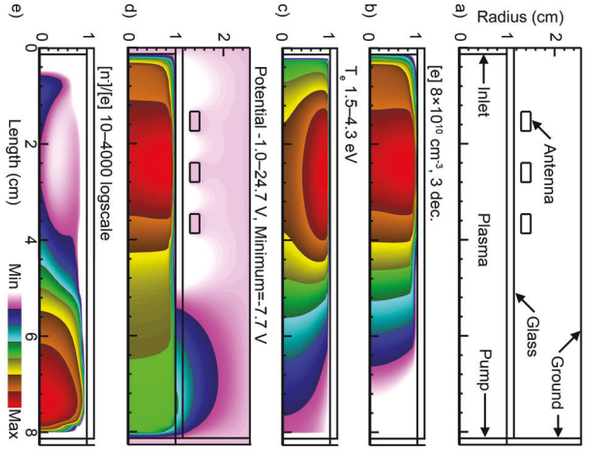

AIP Publishing

Journal of Applied Physics

ACCEPTED MANUSCRIPT

This is the author's peer reviewed, accepted manuscript. However, the online version of record will be different from this version once it has been copyedited and typeset.
PLEASE CITE THIS ARTICLE AS DOI: 10.1063/5.0062255

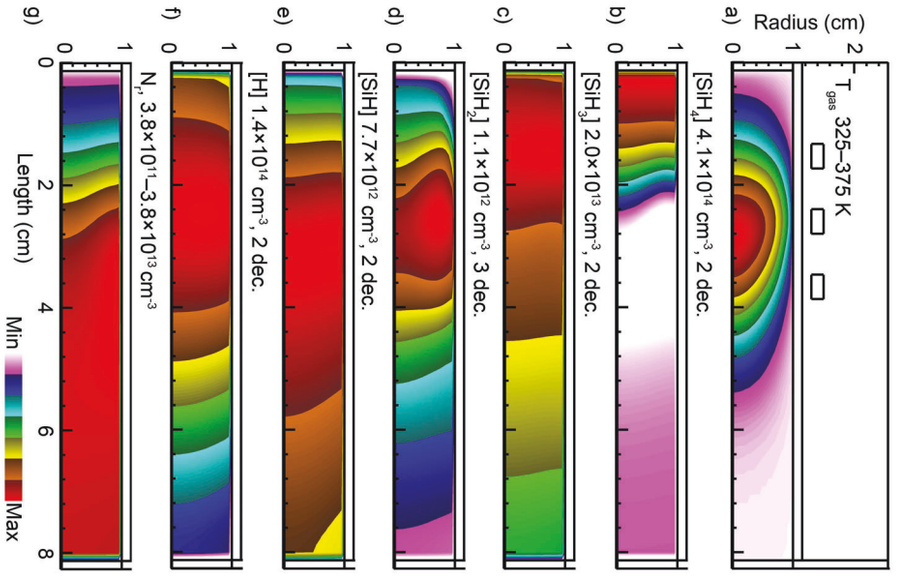

AIP Publishing

Journal of Applied Physics

ACCEPTED MANUSCRIPT

PLEASE CITE THIS ARTICLE AS DOI: 10.1063/5.0062255

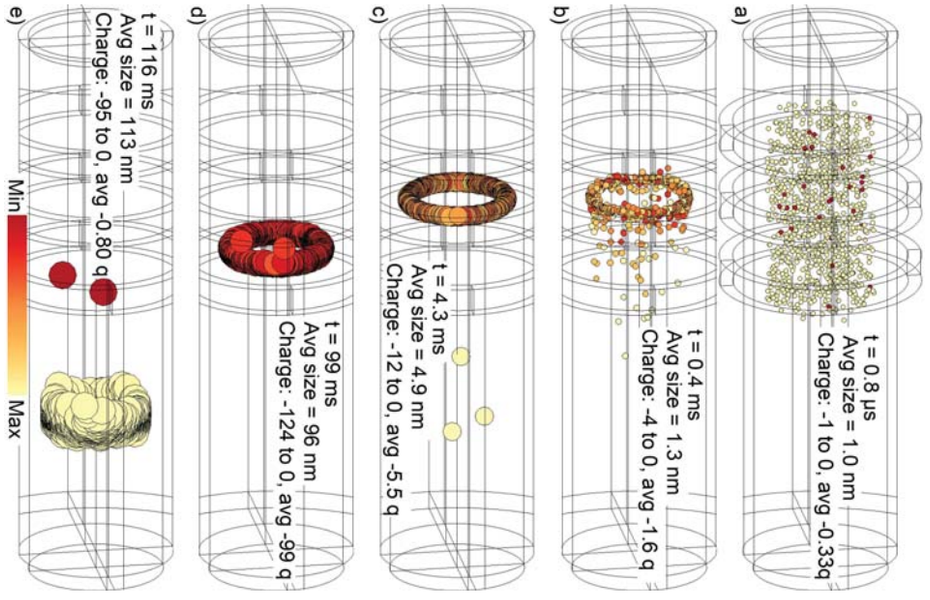

PLEASE CITE THIS ARTICLE AS DOI: 10.1063/5.0062255

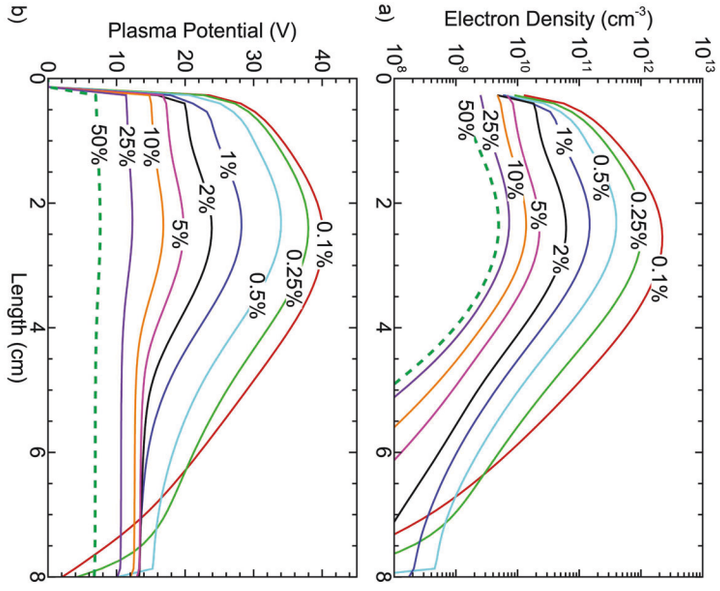

AIP Publishing

Journal of Applied Physics

ACCEPTED MANUSCRIPT

This is the author's peer reviewed, accepted manuscript. However, the online version of record will be different from this version once it has been copyedited and typeset.
PLEASE CITE THIS ARTICLE AS DOI: 10.1063/5.0062255

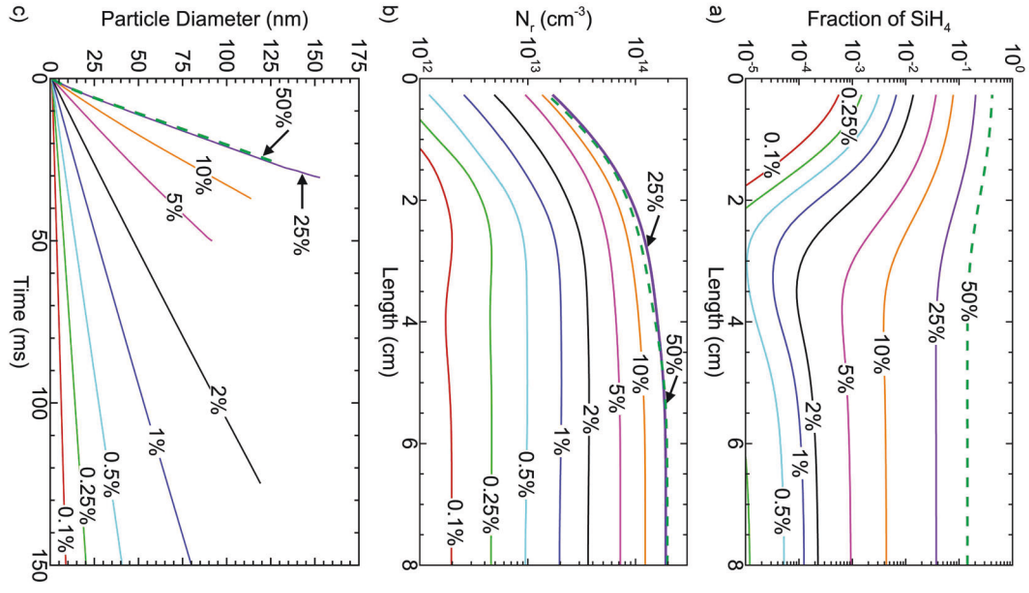

AIP Publishing

Journal of Applied Physics

ACCEPTED MANUSCRIPT

This is the author's peer reviewed, accepted manuscript. However, the online version of record will be different from this version once it has been copyedited and typeset.
PLEASE CITE THIS ARTICLE AS DOI: 10.1063/5.0062255

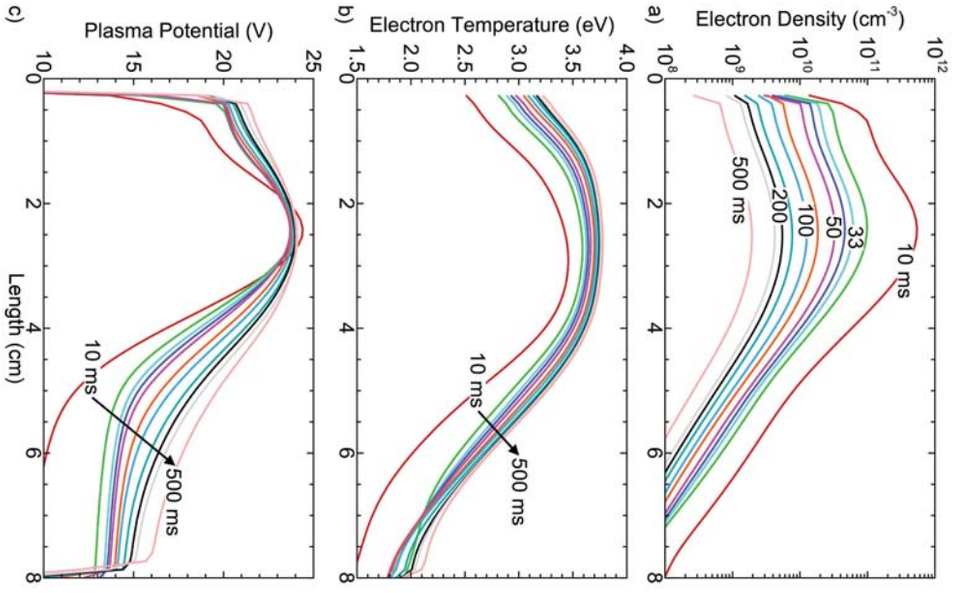

AIP Publishing

Journal of Applied Physics

ACCEPTED MANUSCRIPT

This is the author's peer reviewed, accepted manuscript. However, the online version of record will be different from this version once it has been copyedited and typeset.
PLEASE CITE THIS ARTICLE AS DOI: 10.1063/5.0062255

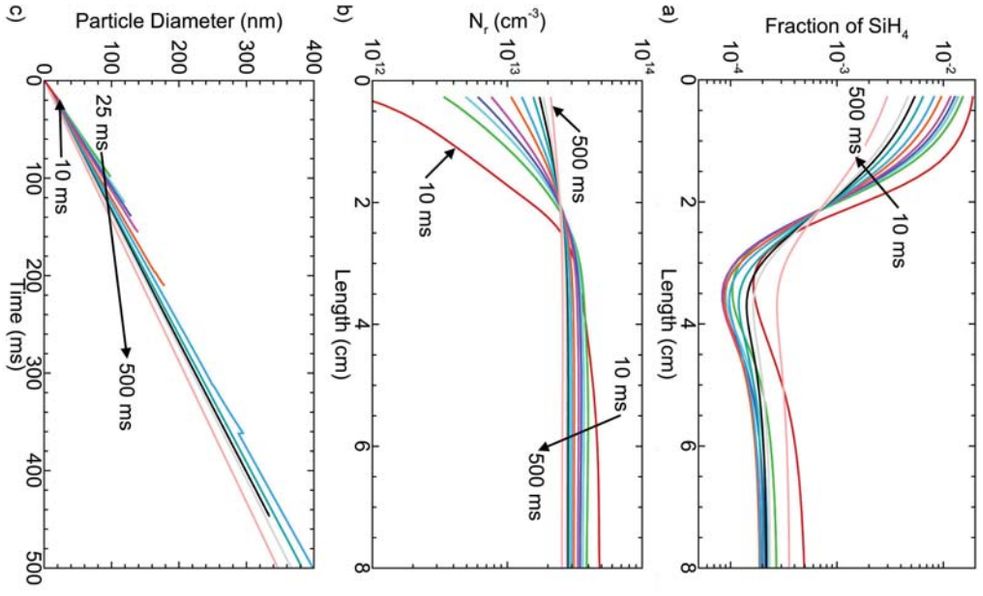

AIP Publishing

Journal of Applied Physics

ACCEPTED MANUSCRIPT

PLEASE CITE THIS ARTICLE AS DOI: 10.1063/5.0062255

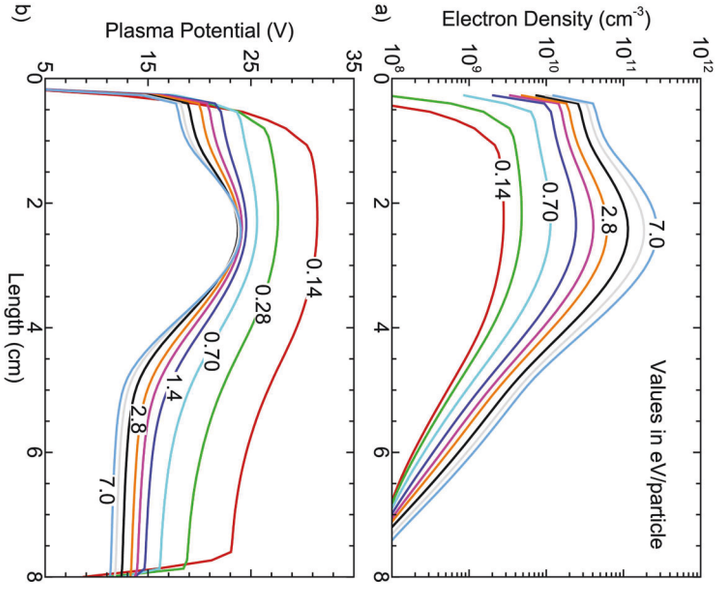

AIP Publishing

Journal of Applied Physics

ACCEPTED MANUSCRIPT

This is the author's peer reviewed, accepted manuscript. However, the online version of record will be different from this version once it has been copyedited and typeset.
PLEASE CITE THIS ARTICLE AS DOI: 10.1063/5.0062255

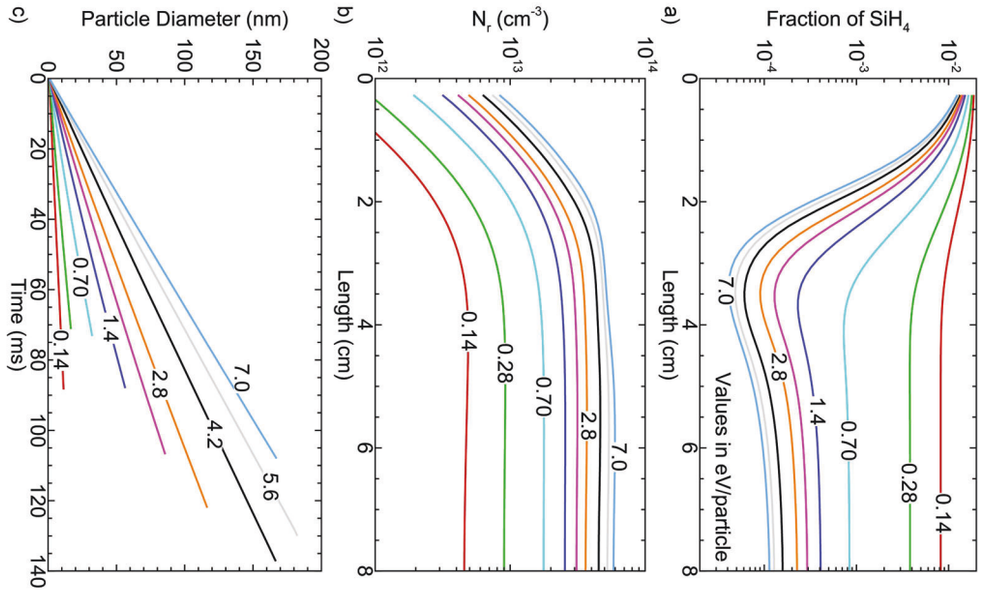

AIP Publishing

Journal of Applied Physics

ACCEPTED MANUSCRIPT

This is the author's peer reviewed, accepted manuscript. However, the online version of record will be different from this version once it has been copyedited and typeset.
PLEASE CITE THIS ARTICLE AS DOI: 10.1063/5.0062255

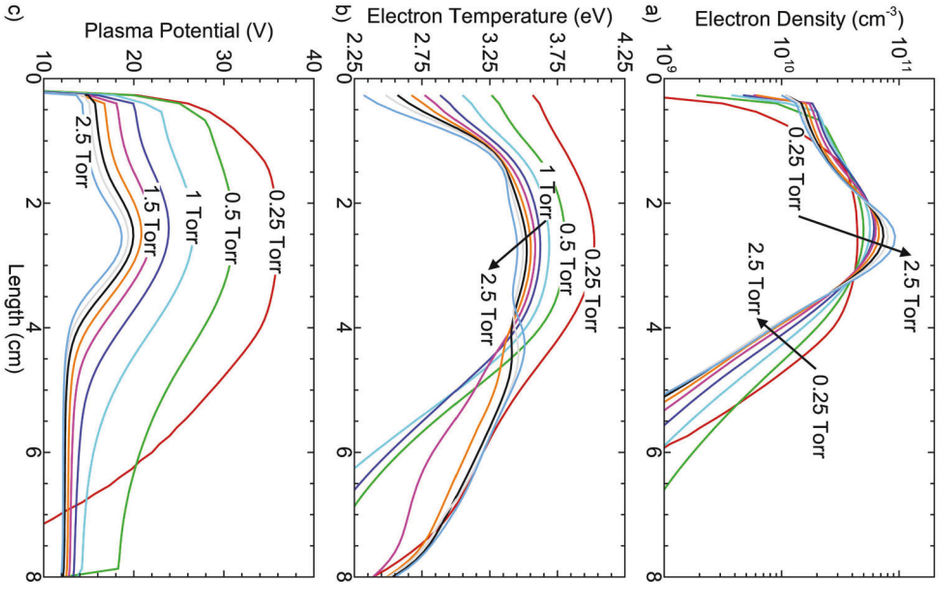

AIP Publishing

Journal of Applied Physics

ACCEPTED MANUSCRIPT

This is the author's peer reviewed, accepted manuscript. However, the online version of record will be different from this version once it has been copyedited and typeset.
PLEASE CITE THIS ARTICLE AS DOI: 10.1063/5.0062255

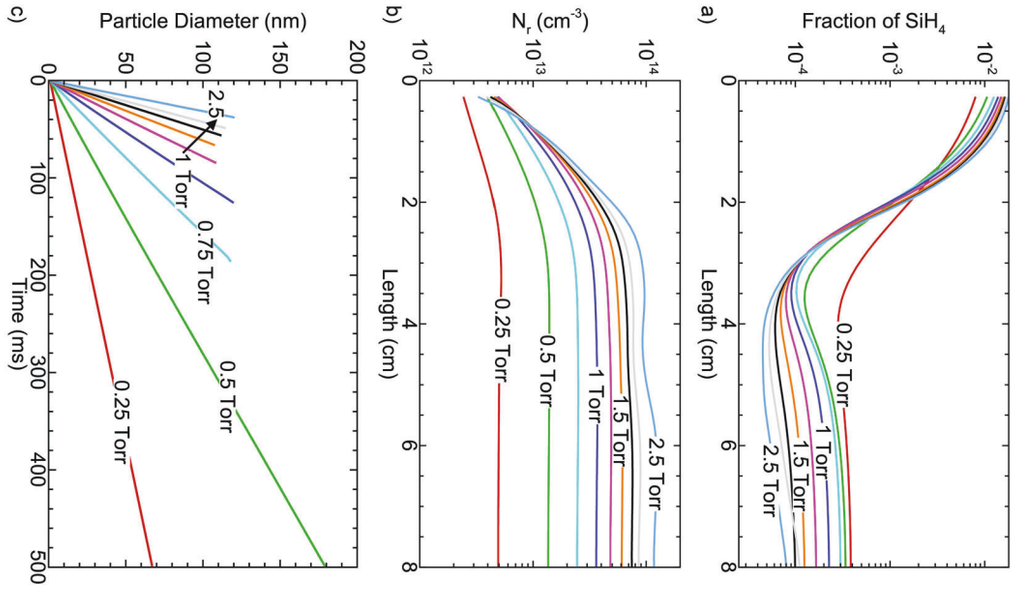

AIP Publishing

Journal of Applied Physics

ACCEPTED MANUSCRIPT

PLEASE CITE THIS ARTICLE AS DOI: 10.1063/5.0062255

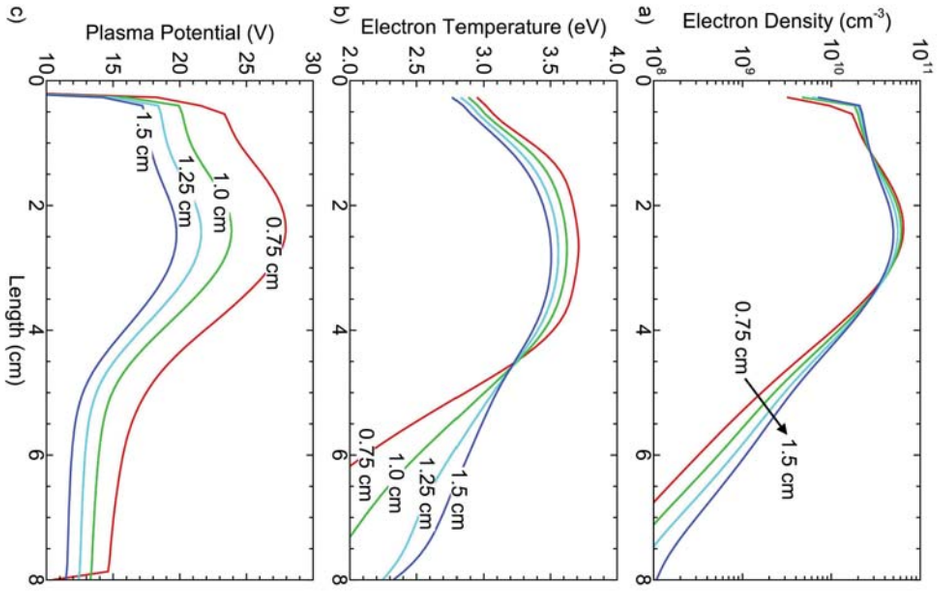

AIP Publishing

Journal of Applied Physics

ACCEPTED MANUSCRIPT

PLEASE CITE THIS ARTICLE AS DOI: 10.1063/5.0062255